Structure and Activity of the N-Terminal Region of the Eukaryotic Cytolysin Equinatoxin II[†]

Alison Drechsler,[‡,§] Cristina Potrich,[||] Jennifer K. Sabo,[‡] Mattia Frisanco,[⊥] Graziano Guella,[⊥] Mauro Dalla Serra,[||] Gregor Anderluh,[#] Frances Separovic,[§] and Raymond S. Norton*[,‡]

The Walter & Eliza Hall Institute of Medical Research, 1G Royal Parade, Parkville, Victoria 3050, Australia, School of Chemistry, University of Melbourne, Melbourne, Victoria 3010, Australia, ITC-CNR, Institute of Biophysics, Via Sommarive 18, 38050 Povo (Trento), Italy, Laboratory of Bioorganic Chemistry, Department of Physics, University of Trento, Via Sommarive 14, 38050 Povo (Trento), Italy, and Department of Biology, Biotechnical Faculty, University of Ljubljana, Vecna pot 111, 1000 Ljubljana, Slovenia

Received October 23, 2005; Revised Manuscript Received December 7, 2005

ABSTRACT: The actinoporins are a family of proteins from sea anemones that lyse cells by forming pores in cell membranes. Sphingomyelin plays an important role in their lytic activity, with membranes lacking this lipid being resistant to these toxins. Pore formation by the actinoporin equinatoxin II (EqTII) proceeds by membrane binding via a surface rich in aromatic residues, followed by translocation of the N-terminal region to the membrane and, finally, across the bilayer to form a functional pore. A key feature of this mechanism is the ability of the N-terminal region to form a stable, bilayer-spanning helix in the membrane, which in turn requires dissociation of the N-terminus from the bulk of the protein and significant extension of the N-terminal helix of native EqTII. In this study the structures of three peptides corresponding to residues 11−29, 11−32, and 1−32, respectively, of EqTII have been investigated by high-resolution nuclear magnetic resonance and Fourier transform infrared spectroscopy. The 32-residue peptide lacks ordered secondary structure in water, but residues 6−28 form a helix in dodecylphosphocholine micelles. Although this helix is long enough to span a bilayer membrane, this peptide and the shorter analogues display limited permeabilizing activity in large unilamellar vesicles and very weak hemolytic activity in human red blood cells. Thus, while the N-terminal region has the structural features required for this unusual mechanism of pore formation, the lack of activity of the isolated N-terminus shows that the bulk of the protein is essential for efficient pore formation by facilitating initial membrane binding, interacting with sphingomyelin, or stabilizing the oligomeric pore.

Equinatoxin II (EqTII)[1] is a pore-forming toxin of 179 residues isolated from the Mediterranean sea anemone *Actinia equina* L (*1*). It is a member of the actinoporin family of sea anemone toxins that function by forming pores in cell membranes via a multistep pathway, which includes membrane binding, conformational change, and oligomerization (*1*). The resulting oligomeric pores, consisting of three or, more likely, four monomers, have a radius of about 1 nm (*2*−*5*) but do not produce a stable structure and have not yet been visualized directly. The actinoporins are highly basic proteins of mass approximately 20 kDa, and their lytic activity is markedly enhanced by the presence of sphingomyelin (SM) (*2*).

The structure of EqTII has been solved in solution (*6*, *7*) and by X-ray crystallography (*8*). EqTII consists of two short helices packed against opposite faces of a β-sandwich structure formed by two five-stranded β-sheets. CD and FTIR studies both detected small increases in β-sheet and α-helical content at the expense of random structure in the presence of unilamellar vesicles (*9*−*11*). Site-directed mutagenesis has shown that at least two regions of EqTII become embedded in lipid membranes, the N-terminal region (residues 10−28) (*12*, *13*) and the surface aromatic cluster including tryptophans 112 and 116 (*12*, *14*, *15*). Indeed, the N-terminal region shows some sequence similarity to melittin, the lytic peptide from honey bee venom (*16*). The current model of pore formation proposes that EqTII binds to the membrane initially via the aromatic-rich region; then the N-terminal region is transferred to the lipid membrane and, finally, across

[†] This work was supported in part by an Australian Research Council Discovery Grant (DP0343883). A.D. acknowledges receipt of an MRS award from the University of Melbourne.

* To whom correspondence should be addressed. E-mail: Ray.Norton@wehi.edu.au. Fax: +61 3 9345 2686. Phone: +61 3 9345 2306.

[‡] The Walter & Eliza Hall Institute of Medical Research.

[§] University of Melbourne.

[||] ITC-CNR, Institute of Biophysics.

[⊥] University of Trento.

[#] University of Ljubljana.

[1] Abbreviations: Chol, cholesterol; DHPC, dihexanoylphosphatidylcholine; DMPC, dimyristoylphosphatidylcholine; DOPC, 1,2-dioleoyl-*sn*-glycero-3-phosphocholine; DOPG, 1,2-dioleoyl-*sn*-glycero-3-[phospho-*rac*-(1-glycerol)]; DPC, dodecylphosphocholine; EqTII, equinatoxin II; HRBC, human red blood cells; $EqTII_{11-29}$, peptide corresponding to residues 11−29 of EqTII; $EqTII_{11-32}$, peptide corresponding to residues 11−32 of EqTII; $EqTII_{1-32}$, peptide corresponding to residues 1−32 of EqTII; FTIR, Fourier transform infrared; HFIP, hexafluoro-2-propanol; LUV, large unilamellar vesicles; PA, egg yolk phosphatidic acid; PC, egg yolk phosphatidylcholine; SM, sphingomyelin; 5-d-SPPC, 5-doxylstearoylpalmitoyl-2-phosphatidylcholine; SUV, small unilamellar vesicles; TFE, trifluoroethanol.

10.1021/bi052166o CCC: $33.50
Published on Web 01/24/2006

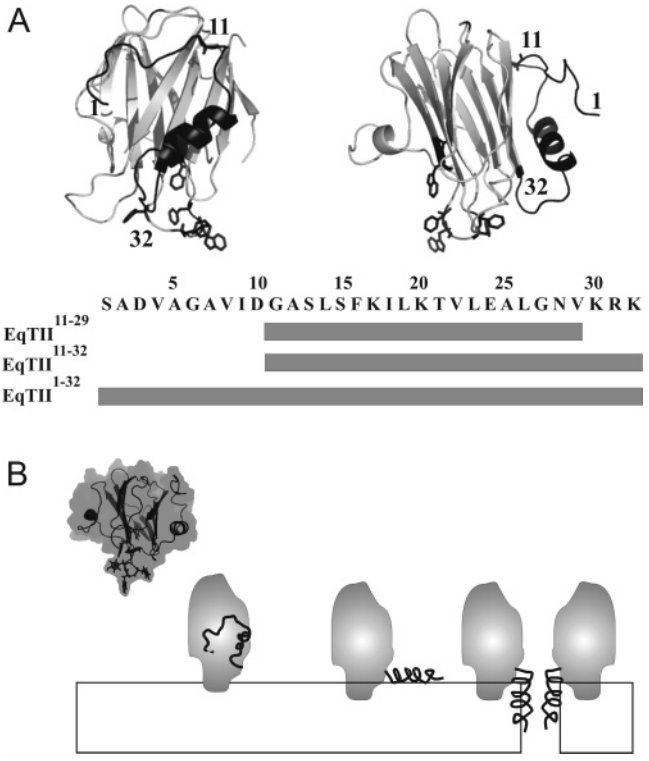

FIGURE 1: (A) Ribbon diagram of the solution structure of EqTII (*7*) showing the location in the structure and amino acid sequence of the N-terminal peptides, $EqTII_{11-29}$, $EqTII_{11-32}$, and $EqTII_{1-32}$. The two views of the structure are related by a 90° rotation about the vertical axis. (B) Schematic of the proposed mechanism of membrane permeabilization by EqTII (*13*). In both (A) and (B) the side chains of several aromatic residues thought to play a role in membrane binding are shown, as follows: Trp112, Trp116, and Trp117 and Tyr108, Tyr110, and Tyr113; Trp117 is largely obscured in the views shown in (A).

the bilayer to form a functional pore (*13*, *15*, *17*). The structural details of the final oligomeric assembly are not known. Nonetheless, it is clear that pore formation by the actinoporins is quite distinct from the mechanisms adopted by various classes of bacterial pore-forming toxins (*18*), many of which attach to membranes via β-sheet structures but then form much larger pores through extensive aggregation and β-strand assembly to produce stable transmembrane β-barrels.

The interaction of EqTII with model lipid membranes composed of PC and SM has also been investigated by solid-state NMR (*19*, *20*). NMR and electron microscopy showed the formation of an isotropic lipid phase in SM-containing bilayers with EqTII (*20*). The toxin enhanced slow motions in the membrane lipids and destabilized membranes containing SM, suggesting a preferential interaction between the toxin and SM.

Implicit in the proposed mechanism of pore formation by EqTII is the assumption that the N-terminal helix in the intact protein remains helical when dissociated from the bulk of the protein and inserted into a lipid environment. In this study we have investigated the structures and lytic activities of a series of peptides corresponding to the N-terminal region of EqTII (Figure 1). This region of EqtII is essential for pore formation, with residues 10−28 forming an α-helical structure in a membrane environment (*13*). N-Terminal truncation reduces EqtII activity and renders the toxin prone to aggregation as a result of exposure to solvent of the nonpolar surface of the underlying β-sheet (*17*). The peptides studied here, corresponding to residues 11−29, 11−32, and 1−32, are indeed helical in model membranes but show very weak permeabilizing and hemolytic activities, implying that the rest of the protein also plays a crucial role in pore formation.

EXPERIMENTAL PROCEDURES

Materials. The N-terminal peptides, $EqTII_{11-29}$, $EqTII_{11-32}$, and $EqTII_{1-32}$, corresponding to residues 11−29, 11−32, and 1−32, respectively, of EqTII were produced by solid-phase synthesis. $EqTII_{11-29}$ was synthesized using a ResPep synthesizer (Intavis, Germany) with Fmoc chemistry. $EqTII_{11-32}$ was obtained from Genemed Synthesis (San Francisco, CA) and further purified by reversed-phase HPLC on a C18 column (Phenomenex). $EqTII_{1-32}$ was purchased from INBIOS (Pozzuoli, NA, Italy) and Mimotopes (Melbourne, Australia). All peptides exhibited their expected molecular masses of 1948, 2359, and 3257 Da, respectively, by MALDI-TOF MS.

Lipids used were dodecylphosphocholine-$^2H_{38}$ (DPC-$^2H_{38}$) from Cambridge Isotope Laboratories (Andover, MA) and cholesterol (Chol), dihexanoylphosphatidylcholine (DHPC), dimyristoylphosphatidylcholine (DMPC), egg yolk phosphatidylcholine (PC), egg yolk phosphatidic acid (PA), 1,2-dioleoyl-*sn*-glycero-3-phosphocholine (DOPC), 1,2-dioleoyl-*sn*-glycero-3-[phospho-*rac*-(1-glycerol)] (DOPG), porcine brain sphingomyelin (SM), and 5-doxylstearoylpalmitoyl-2-phosphatidylcholine (5-d-SPPC) from Avanti Polar Lipids (Alabaster, AL). Calcein and Sephadex G-50 were from Sigma (Milan, Italy), Triton X-100 was from Merck (Milan, Italy), and Prionex (porcine hydrolyzed collagen of average mass 20 kDa) was from Pentapharm Ltd. (Basel, CH). DMSO-$^2H_6$ (99.9%) and ^2H_2O were purchased from Merck (Germany), and trifluoroethanol-$^2H_3$ (TFE-$^2H_3$) was from Cambridge Isotope Laboratories (Andover, MA).

Fourier Transform Infrared (FTIR) Spectroscopy. FTIR spectroscopy was used to assess the secondary structure of peptides in solution by analysis of the amide I′ band, as described previously (*11*). Samples were deposited on 10-reflection germanium crystals (45° cut) and gently dried by nitrogen flushing. Spectra of hydrated and deuterated films were collected, in an ATR geometry, using a FTS 185 spectrometer (Bio-Rad), with a MCT detector. To estimate the secondary structure content, the amide I′ band in the region 1700−1600 cm^{-1} was deconvoluted into a set of Lorentzian components whose frequencies were assigned to different structural elements in the standard way (*11*). In particular, we used the following assignments: band at 1680 ± 3 cm^{-1}, β-turn; bands in the region 1656−1646 cm^{-1}, α-helix; band at 1640 ± 5 cm^{-1}, random coil; band around 1610 ± 5 cm^{-1}, side chain contribution. In addition, we observed two bands, a major one around 1624 cm^{-1} and a minor one at 1692 cm^{-1}, which are typical of aggregated peptide in an extended configuration and correspond to strong inter- and intrastrand interactions (*21*). This set of Lorentzians was used to fit the original spectrum, and the resulting relative areas were taken as the proportion of the corresponding structures present. The curve fit was used to calculate the percentage of peptide aggregation. The aggregated peptide is represented by the bands around 1624 and 1692 cm^{-1} and the nonaggregated by all of the remaining amide I′ components in the region 1630−1690 cm^{-1}.

Lipid Vesicle Preparation. Large unilamellar vesicles (LUVs) were prepared as described previously (*5*) by extruding a solution of multilamellar liposomes prepared in the presence of 80 mM calcein (pH 7, adjusted by NaOH) and subjecting it to six cycles of freezing and thawing. A pneumatic two-syringe or manual extruder (LiposoFast—Pneumatic, AVESTIN) was used, equipped with two stacked polycarbonated filters (Millipore) with 100 nm pores (*22*). Thirty-one passages were performed each time. Lipid compositions used initially were DOPC, DOPC:SM, 1:1 (mol/mol), and DOPC:DOPG, 1:1 (mol/mol) and, for more thorough screening of pH effects, PA, PA:PC, 1:1 (mol/mol), PA:PC:Chol, 1:1:1 molar ratio, and PC. The initial lipid concentration was 5 mg/mL. To remove untrapped calcein, the vesicles were spun through minicolumns (Strata; Phenomenex) loaded with Sephadex G-50 (medium). Vesicle dimensions and homogeneity were routinely estimated by dynamic light scattering using a Malvern Zeta-Sizer 3 apparatus (Malvern) as described previously (*23*).

Permeabilization of Large Unilamellar Vesicles. Vesicle permeabilization was assayed initially in a 1.5 mL cuvette (Jasco FP-750 fluorimeter), where permeabilization properties of the peptide $EqTII_{1-32}$ were compared to those of the wild-type EqTII. Lipid vesicles at 25 μM final concentration were stirred at 25 °C, then toxin or a peptide at the desired lipid/toxin (L/T) ratio was added, and fluorescence was followed for 20 min. The maximal release was obtained by the addition of 2 mM Triton X-100 at the end of the assay. The excitation and emission wavelengths were 485 and 520 nm, respectively; both slits were set to 5 nm. Peptides were assayed in a fluorescence microplate reader (Fluostar Galaxy; BMG) to test the effect of pH and various lipid compositions on the activity of all three peptides. Excitation and emission were set at 480 and 540 nm, respectively. Peptides at various concentrations in buffer (100 μL) were dispensed in a 96-well microplate, followed by addition of 100 μL of calcein-loaded LUVs at a final lipid concentration of 6 μM. The time course of calcein release was then recorded as described previously (*24*). The buffers were 140 mM NaCl, 1 mM EDTA, and 20 mM MES for pH values ranging from 4 to 6, 20 mM Hepes for pH 7, and 20 mM Tris-HCl for pH 8 and 9. The percentage of calcein release [R (%)] was calculated as follows:

$$R\,(\%) = (F_{fin} - F_{in})/(F_{max} - F_{in}) \times 100$$

where F_{in} and F_{fin} represent the initial and final (steady-state) values of fluorescence, respectively, before and after peptide addition. F_{max} is the fluorescence after the addition of 1 mM Triton X-100. C_{50} is the peptide concentration causing 50% of calcein release.

Light Scattering. The variation in static light scattering was measured at 300 nm for both excitation and emission wavelengths with a spectrofluorimeter (FluoroMax SPEX; Horiba Jobin Yvon), using 100 μL quartz cuvettes. Excitation and emission slits were set at 2 nm. The effect of increasing concentrations of peptide on PA:PC vesicles (12.5 μM) was tested in 140 mM NaCl, 1 mM EDTA, and 20 mM Tris-HCl at pH 8.

Hemolytic Activity. Hemolytic activity was measured turbidimetrically at 650 nm with a microplate reader (UVmax from Molecular Devices, Sunnyvale, CA) supported by the computer program SOFTmax, as described previously (*24*). Briefly, human red blood cells (HRBC) were prepared from fresh heparinized blood by washing three times (700*g* for 10 min) and resuspending in saline buffer: 140 mM NaCl and 10 mM Tris-HCl, with the pH adjusted to 6, 7, or 8. Finally, the concentration of HRBC was adjusted with buffer to give an apparent final absorbance of 0.1 at 650 nm, corresponding to about 1.2×10^7 cells/mL. Peptides were 2-fold serially diluted in the appropriate buffer using flat-bottom, 96-well microplates, previously treated for 30 min with 0.1 mg/mL Prionex to saturate the nonspecific protein binding sites on the plastic, which can reduce free peptide concentration. One volume of HRBC was added to each well and the time course of hemolysis was followed for 30 min at room temperature. Percentage hemolysis was determined as follows:

$$\text{hemolysis}\,(\%) = (A_{max} - A_{fin})/(A_{max} - A_{min}) \times 100$$

where A_{max} and A_{min} represent the absorbance values for intact and completely hemolyzed HRBC, respectively, and A_{fin} is the final absorbance value.

NMR Sample Preparation. Samples of $EqTII_{11-29}$ for NMR were prepared at a concentration of approximately 4 mM in either 100% DMSO-$^2H_6$ or 90% (v/v) H_2O/10% ^2H_2O. Samples of $EqTII_{1-32}$ were prepared in 95% H_2O/5% ^2H_2O, 40% TFE-$^2H_3$/60% H_2O, or 125 mM DPC-$^2H_{38}$ in 95% H_2O/5% ^2H_2O containing 1.9 mM sodium azide to final peptide concentrations of approximately 1.0, 0.8, and 1.4 mM and pH values of 5.1, 5.6, and 5.1, respectively. pH was adjusted without buffers and measured at room temperature, with no allowance made for isotope effects.

NMR Spectroscopy. NMR spectra of $EqTII_{11-32}$ were acquired on a Bruker Avance 400 NMR spectrometer running XWINNMR (1.3) and processed using Bruker TOPSPIN (version 1.3) software. TOCSY spectra were recorded with a 2 ms trim pulse preceding the MLEV-17 spin-lock of 60 ms and NOESY spectra with mixing times of 50, 250, and 600 ms. Proton DQF-COSY, NOESY, and TOCSY spectra were acquired with a spectral width of 5000 Hz, 4096 complex points in the ω_2 dimension and 1024 in the ω_1. Water suppression was accomplished by presaturation, and all spectra were recorded with time-proportional phase incrementation (TPPI). Chemical shifts were referenced to the residual solvent signal at 2.50 ppm for DMSO and 4.72 ppm for H_2O at 25 °C. $^1H-^{13}C$ HSQC spectra (*25*) were recorded to obtain ^{13}C chemical shifts.

Temperature coefficients for amide protons were determined from TOCSY spectra acquired at 5 °C intervals over the range 25−45 °C for DMSO and 25 and 30 °C for water. All other spectra were recorded at 30 °C for the DMSO sample and 25 °C for water.

All spectra of $EqTII_{1-32}$ were acquired on a Bruker DRX-600 spectrometer. One-dimensional ^1H spectra were obtained over a range of different temperatures and pH values to compare chemical shift dispersion, as follows: 90% H_2O/10% ^2H_2O at pH 5.1 and 25 °C, in 10%−50% TFE-$^2H_3$ and 40% TFE-$^2H_3$ between pH 4.1 and 6.0 and in DPC-$^2H_{38}$ at pH 5.5, at 5 °C intervals between 25 and 45 °C. The following 2D homonuclear spectra were acquired on $EqTII_{1-32}$ in DPC-$^2H_{38}$: TOCSY with spin-lock times of 10, 20, and 40 ms, NOESY with mixing times of 100, 150, and 200 ms,

DQF-COSY and E-COSY spectra, all in the phase-sensitive mode using the time-proportional phase incrementation method. A $^1H-^{13}C$ HSQC spectrum (*25*) was acquired at natural abundance. Water was suppressed either by pulsed field gradients employing the WATERGATE method, incorporating a 3-9-19 refocusing pulse sequence (*26*), or by selective, low-power irradiation of the water signal during the relaxation delay (typically 1.8 s) and during the mixing time in NOESY experiments. Homonuclear 2D spectra were acquired with 400−600 t_1 increments, 96−128 scans per increment, and 4096 data points. Sine-squared window functions, phase shifted by 60−90°, were applied in both dimensions prior to Fourier transformation. Spectra were processed using XWINNMR (Bruker Biospin) and analyzed using XEASY (*27*).

Backbone amide exchange was measured by dissolving the sample in ^2H_2O at pH 4.8 and recording a series of 1D and TOCSY spectra at 35 °C. Once exchange was complete, E-COSY, 200 ms NOESY, and $^1H-^{13}C$ HSQC spectra were acquired.

Structural Constraints. Distance restraints for $EqTII_{1-32}$ in DPC-$^2H_{38}$ micelles were obtained from 100 and 200 ms NOESY spectra at pH 5.0 and a 200 ms NOESY in DPC-$^2H_{38}$/^2H_2O at pH 4.8. $^3J_{HNH\alpha}$ coupling constants were measured from a DQF-COSY and converted to dihedral restraints ($^3J_{HNH\alpha} > 8$ Hz, $\phi = -120 \pm 30°$; $^3J_{HNH\alpha} < 6$ Hz, $\phi = -60 \pm 30°$); if a positive ϕ angle could be excluded on the basis of NOE data (*28*), ϕ angles were restricted to the range −180 to 0°. χ^1 angles were determined on the basis of analysis of a 100 ms NOESY spectrum. ϕ, ψ, and χ^1 angles were predicted using TALOS (*29*) from $^{13}C^{\alpha}$, $^{13}C^{\beta}$, and $^1H^{\alpha}$ chemical shifts and restricted if similar to those already existing in the structures. Amide protons with resonances that were still visible in a 2D TOCSY acquired 2 h after dissolution in ^2H_2O, and/or with a temperature coefficient of magnitude 4 ppb/°C or less, were included in hydrogen bond restraints after initial structure calculations in X-PLOR defined their acceptors.

Structure Calculations. Structural calculations were performed in CYANA (*30*), using a peak list derived from the NOESY spectra described above. Intensities for each peak were calibrated using the conventional CALIBA (*31*) script supplied with CYANA. A family of 100 structures was calculated using torsion angle dynamics until no dihedral violations greater than 5° or NOE violations greater than 0.2 Å were observed across the family. The final NOE and dihedral restraint lists from CYANA were then used to calculate a family of 100 structures in XPLOR-NIH (*32*) using the standard distance geometry and simulated annealing scripts. Fifty-three structures were selected for water refinement, based on their target function; a water box was built around the molecule and then energy minimized on the basis of NOE and dihedral restraints and the geometry of bonds, angles, and impropers. A final family of 20 structures was then chosen for further analysis based on their energy and an absence of disallowed residues in the Ramachandran plot. Structures were analyzed using the programs PROCHECK (*33*) and MOLMOL (*34*). Structural figures were prepared using MOLMOL, PyMOL (DeLano Scientific LLC), and INSIGHT II (MSI).

Translational Diffusion. Translational diffusion rates were measured at 45 °C using a pulsed field gradient longitudinal eddy-current delay pulse sequence (*35*, *36*). A series of 12 or 34 diffusion-weighted spectra for either DPC-$^2H_{38}$ alone or peptide in DPC-$^2H_{38}$, respectively, were recorded in a 2D manner with a recycle time of 5 s and 64 scans. Translational diffusion coefficients, *D*, were obtained using the program Simfit (Bruker) and averaged over all peaks selected as described previously (*36*). The agreement across fits from different peaks in the same sample was usually better than 10%. For $EqTII_{1-32}$ in aqueous solution the values for individual peaks were more scattered, and the fits to a single exponential were poorer, perhaps as a result of the presence of a mixture of species with different diffusion times; because structural studies were not undertaken on this sample, this was not investigated further.

Paramagnetic Relaxation Agents. The location of $EqTII_{1-32}$ in DPC-$^2H_{38}$ micelles was investigated by comparing the changes in intensities of intraresidue NH−H^{α} NOESY cross-peaks upon addition of the paramagnetic agents Mn^{2+} and 5-doxylstearoylpalmitoyl-2-phosphatidylcholine (5-d-SPPC). Mn^{2+} affects the resonances of the DPC-$^2H_{38}$ phosphocholine headgroup, while the nitroxide-containing lipid affects resonances throughout the micelle (*37*). Samples were prepared by addition of either Mn^{2+} (as $MnCl_2$ in H_2O) or 5-d-SPPC (in chloroform-$^2H_3$) to $EqTII_{1-32}$ in DPC-$^2H_{38}$ micelles at pH 5.0. The paramagnetic agent was titrated into the sample, and 1D spectra were acquired after each addition to detect spectral changes. NOESY spectra (mixing time 100 ms) were acquired at 45 °C at low (1:5) and high (1:10) peptide:Mn^{2+} and low (5.7:1) and high (2.9:1) peptide:5-d-SPPC ratios. Intensities of NH−H^{α} cross-peaks were calculated in XEASY for the nil, low, and high concentrations. The remaining relative amplitude (RA) was calculated for the NH−H^{α} NOESY cross-peak of each residue at the two concentrations of the paramagnetic agent. RA is defined as

$$RA = N(A_{paramag}/A_0)$$

where $A_{paramag}$ and A_0 are the amplitudes of cross-peaks measured in the presence and absence of the paramagnetic probe, respectively. *N* is the normalizing factor, which results in the least affected cross-peak remaining at a relative amplitude of 1 (*38*). The peptide structure was maintained upon addition of either paramagnetic agent, based on the absence of chemical shift perturbations.

RESULTS

Lytic Activity of Peptides. The hemolytic activity of the peptides toward human red blood cells was measured initially, as this is one of the standard tests for pore-forming activity of actinoporins (*2*, *5*). Activity was measured at pH values of 6, 7, and 8. The longer N-terminal EqTII peptides $EqTII_{1-32}$ and $EqTII_{11-32}$ showed no activity on erythrocytes under any conditions. $EqTII_{11-29}$ was very weakly active, showing only about 10% hemolysis at a concentration of 25 μM at pH 7 and 8 (data not shown). As this activity was roughly 3 orders of magnitude weaker than that of EqTII, it was not regarded as significant (*2*, *39*).

The activity of the longest peptide, $EqTII_{1-32}$, was then checked in a large unilamellar vesicle (LUV) permeabilization assay with a standard lipid mixture (DOPC:SM, 1:1) used for assaying actinoporin activity. This composition is by far the most sensitive to the actinoporins (*2*, *5*), but the

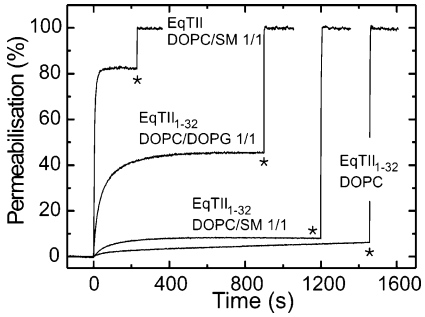

FIGURE 2: Calcein release from large unilamellar liposomes (LUVs) of different composition. Calcein fluorescence was excited at 495 nm, and emission was followed at 520 nm for at least 20 min at 25 °C. LUV (final lipid concentration 25 μM) were stirred in 140 mM NaCl, 20 mM Tris-HCl, and 1 mM EDTA, pH 8.5. Peptide $EqTII_{1-32}$ or EqTII was then added at final concentrations of 5 or 1 μM, respectively; the final lipid/$EqTII_{1-32}$ molar ratio was therefore 5, and for EqTII 25. The maximal permeabilization was achieved at the end of the assay by the addition of 2 mM Triton X-100 (denoted by an asterisk).

peptide showed no activity. At a lipid:peptide ratio of 25 the permeabilization was only 2 ± 2% (average ± SD; n = 2 for all experiments; data not shown), compared with 78 ± 7% for native EqTII at the same molar lipid:protein ratio (Figure 2). At a lipid:peptide ratio of 5, the peptide still showed only very weak activity of 9 ± 2% (Figure 2). The permeabilization activity of the peptide on pure DOPC LUVs was also very low, at 3 ± 3% (Figure 2). These results indicate that the peptides do not behave like melittin, which at these lipid:peptide ratios would completely lyse membranes by a detergent-like mechanism (*19*). As two of the three peptides have a cluster of C-terminal positive charges (Figure 1), permeabilization activity was tested on membranes containing negatively charged lipids. There was indeed more release observed, approximately 43 ± 3% from DOPC:DOPG (1:1) LUVs (Figure 2). This result prompted a more detailed analysis of all three peptides at various pHs and against other lipid mixtures that contained negatively charged lipids. All three peptides showed the highest activity at basic pH (Figure 3). The activity on vesicles composed of pure PC or PA:PC:Chol was negligible, but lytic activity was always observed with pure PA or PA:PC LUVs. Calcein release was maximal for $EqTII_{11-32}$ with LUV made from pure PA. This activity was similar to that of $EqTII_{1-32}$ when PC:PA vesicles were used ($1/C_{50}$ between 2 and 2.5 μM^{-1} at pH 9; Figure 3A). The strong difference in activity of $EqTII_{11-32}$ for the two types of vesicles can be attributed to the presence of a net positive charge in $EqTII_{11-32}$, while $EqTII_{1-32}$ is globally neutral and thus showed similar activity in both types of membranes. $EqTII_{11-29}$ instead showed poor vesicle permeabilization, probably because of the absence of the KRK sequence. This very basic region could favor the interaction of the peptides with a negatively charged lipid such as PA. In fact, when only 30% PA was included in the liposome composition (PA:PC:Chol), no activity was detected.

Light Scattering. Light scattering measurements were then undertaken to establish whether the observed release of calcein from LUVs was due to a detergent-like effect or channel-like activity of the peptides. When $EqTII_{1-32}$ was added to PA:PC LUVs at pH 8 (Figure 4), light scattering decreased initially up to 43% as the peptide concentration

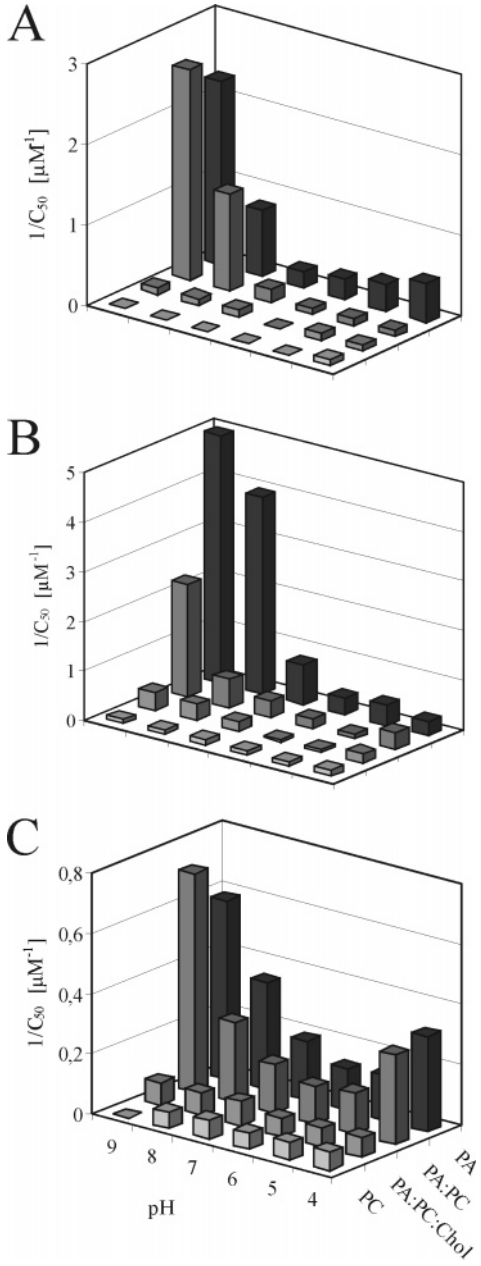

FIGURE 3: Permeabilizing effect of the N-terminal EqTII peptides on vesicles (LUVs) of different composition and at different pH:. (A) $EqTII_{1-32}$, (B) $EqTII_{11-32}$, and (C) $EqTII_{11-29}$. Activities are shown as $1/C_{50}$, with units of μM^{-1}.

was increased to 14 μM. However, when the peptide concentration was increased above 14 μM (i.e., higher than $C_{peptide}/C_{lipid}$ = 1.12), an increase in light scattering was observed, indicative of vesicle aggregation. From a comparison of calcein release and light scattering from the LUVs following peptide addition, the data are consistent with channel formation. Interestingly, calcein release was maximal before the light scattering minimum, most likely due to changes in vesicle shape at these high peptide concentrations rather than lysis, as the subsequent increase in scattering of the LUVs indicates vesicle fusion or aggregation. By contrast, when $EqTII_{11-32}$ was added, the LUVs showed a decrease in light scattering until 4 μM concentration ($C_{peptide}/C_{lipid}$ = 0.32), followed by a very rapid change in light scattering as aggregation proceeded. Following addition of $EqTII_{11-29}$ to LUVs, the light scattering decreased until the peptide

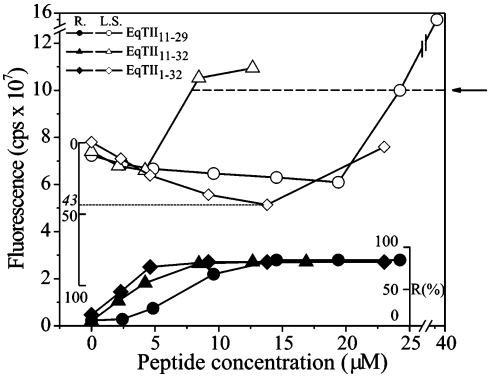

FIGURE 4: Calcein release (R, R%) and light scattering (L.S., %) of the N-terminal EqTII peptides on LUV PA:PC at pH 8. The dashed line denoted by an arrow indicates the cps value over which the peptide solutions showed high turbidity, visible by eye. The 100% value of light scattering corresponds to a complete micellization of the liposomes alone obtained after treatment with Triton X-100.

concentration was 19.1 μM ($C_{peptide}/C_{lipid} = 1.52$), indicating channel formation in the vesicles, but then increased even faster than in the $EqTII_{11-32}$ case, the solution becoming turbid because of rapid aggregation of the LUVs.

Peptide Secondary Structure in Solvent. FTIR spectra were recorded for the peptides dissolved in various solvents. Secondary structure was estimated by deconvolution and curve fitting with a set of Lorentzian components attributed to different structural elements (Figure 5 and Table 1). Analysis of the amide I′ band for $EqTII_{1-32}$ in methanol suggested the presence of a large aggregated β-sheet component (about 28%) which was subtracted from the spectra in order to determine the secondary structure of the nonaggregated peptide. The same procedure was adopted for the other two peptides. The nonaggregated portion of $EqTII_{1-32}$ in methanol showed about 27% α-helix and about 56% β-structure. $EqTII_{11-32}$ was mainly α-helical (about 65%) in methanol and no aggregated structure was detected, probably because the absence of the first 10 residues allows the KRK residues to render the peptide more soluble. $EqTII_{11-29}$ was also mainly α-helical (54%) in hexafluoro-2-propanol (HFIP), although a significant proportion (about 30%) was aggregated, possibly due to the absence of the KRK sequence.

NMR spectra of $EqTII_{11-32}$ were also acquired, as shown in Figures S1−S5 in Supporting Information. The sequence-specific ^1H and $^{13}C^{\alpha}$ resonance assignments for $EqTII_{11-29}$ in DMSO-$^2H_6$ at 30 °C are summarized in Table S1 in Supporting Information. The observed NOEs were predominantly intraresidue and sequential, indicating that $EqTII_{11-29}$ in DMSO does not adopt a stable conformation under these conditions. This was also the case for the peptide in both DMSO and 90% H_2O/10% ^2H_2O over the temperature range 25−45 °C (Figure S6). Figure 6 shows the deviations of H^{α} chemical shifts from random coil values for the peptide in DMSO and water. The slight upfield deviations suggest a propensity for helix formation by this peptide but no stable helical structure under these conditions, unlike the FTIR spectra of the peptide in HFIP, which indicated mainly α-helical structure.

NMR Spectroscopy of EqTII$_{1-32}$. ^1H spectra of $EqTII_{1-32}$ in aqueous solution showed limited chemical shift dispersion,

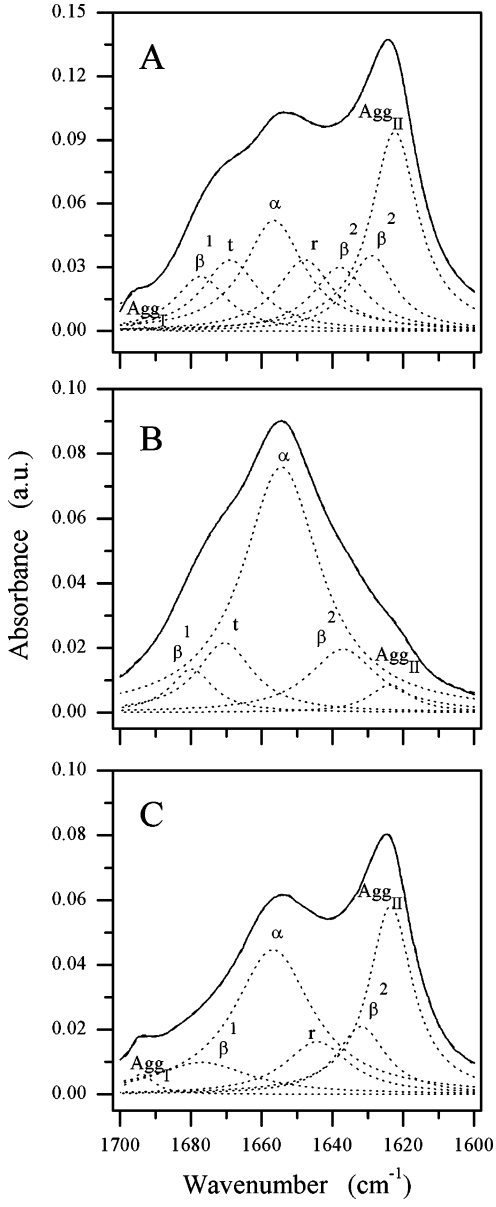

FIGURE 5: Infrared attenuated total reflection spectra of the N-terminal EqTII peptides: (A) $EqTII_{1-32}$, (B) $EqTII_{11-32}$, and (C) $EqTII_{11-29}$. Analysis of the amide I′ band of deuterated films deposited from methanol (A, B) or HFIP (C) solutions. The original spectrum (solid line) was deconvoluted and curve fitted to resolve the component frequencies. The corresponding Lorentzian bands are reported as dotted lines, and their sum (thick dashed line) was superimposed onto the original spectrum. Bands indicated as Agg_I and Agg_{II} derive from aggregated peptide and were excluded from the secondary structure estimation. The other bands are t (β-turn), α (α-helix), β^1 and β^2 (β-sheet), and r (random coil). The evaluated percentages of secondary structures are reported in Table 1.

implying that this peptide did not adopt a stable secondary structure under these conditions. The diffusion coefficient in water was 3.36×10^{-10} m^2/s at 25 °C. Addition of TFE, a solvent known to stabilize helical structure in peptides, increased the dispersion of the amide peaks, presumably because of helix formation, with spectral dispersion reaching a plateau around 40% TFE. However, variations in peak position over time suggested that the structure was not stable in aqueous TFE.

One-dimensional spectra of the peptide in DPC-$^2H_{38}$ micelles were well dispersed and stable with time. The molar

Table 1: FTIR Spectroscopic Determination of the Secondary Structure of N-Terminal Peptides of EqTII in Methanol and HFIP

	% secondary structure[a]					
peptide	β^1	β^2	t	α	r	Agg
$EqTII_{1-32}$	11.3 ± 0.5	28.9 ± 0.5	16.3 ± 0.5	27.0 ± 0.5	16.5 ± 0.5	27.6 ± 0.5
$EqTII_{11-32}$	6.6 ± 0.5	15.0 ± 0.5	13.7 ± 0.5	64.7 ± 0.5		4.0 ± 0.5
$EqTII_{11-29}$	12.9 ± 0.5	16.7 ± 0.5		53.7 ± 0.5	16.7 ± 0.5	30.1 ± 0.5

[a] Value are the mean ± SD. β^1, antiparallel β-sheet; β^2, parallel and antiparallel β-sheet; t, β-turn; α, α-helix; r, random coil; Agg, aggregated (sum of $Agg_I + Agg_{II}$; see Figure 5). The percentages of the secondary structures are calculated after subtracting the contribution from the aggregated component. $EqTII_{1-32}$ and $EqTII_{11-32}$ were examined in methanol, and $EqTII_{11-29}$ was examined in HFIP.

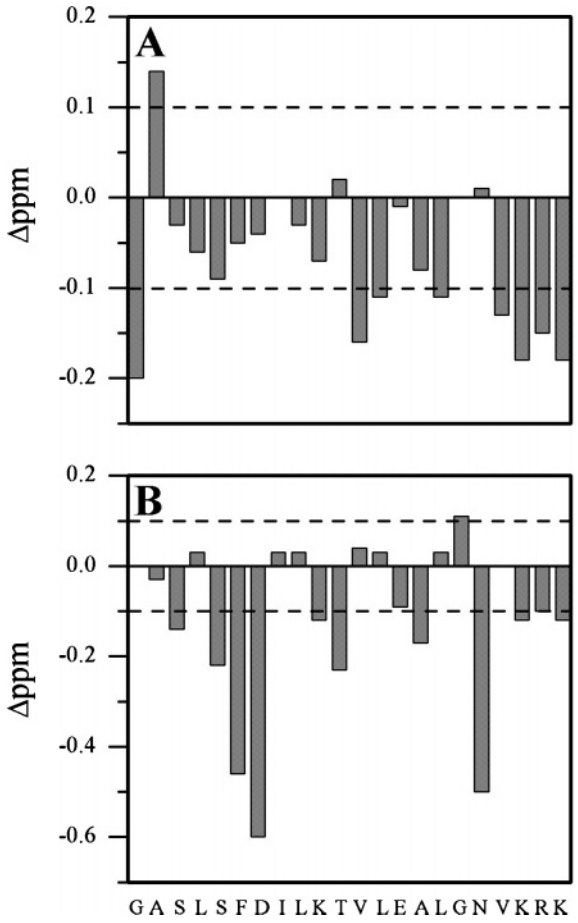

FIGURE 6: Deviations of H^α chemical shifts from random coil values (*51*) for $EqTII_{11-32}$ in (A) DMSO-$^2H_6$ and (B) 90% H_2O/10% ^2H_2O.

ratio of peptide to DPC-$^2H_{38}$ was around 1:90, equivalent to a 1.5 molar excess of micelles over peptide, assuming 60 DPC-$^2H_{38}$ molecules per micelle (*40*). The diffusion coefficients of the peptide and DPC-$^2H_{38}$ in this sample were 2.9×10^{-10} and 2.86×10^{-10} m^2/s, respectively, at 45 °C, indicating that the peptide is predominantly bound to the micelles. The diffusion coefficient of DPC in the absence of peptide was 3.64×10^{-10} m^2/s; this value is higher than for peptide-containing micelles, presumably due to a reduction in either the Perrin shape factor or the hydrodynamic radius of the micelle (*41*). The 20% slower diffusion of the peptide−micelle complex is probably largely a result of its increased size compared with free micelles, and it seems that the peptide is not causing significant micellar aggregation.

Assignments and Structural Restraints. Sequence-specific resonance assignments for $EqTII_{1-32}$ in DPC-$^2H_{38}$ micelles at pH 5.1 and 45 °C are tabulated in Table S2 in Supporting Information and have been deposited in BioMagResBank (*42*) with accession number 6808. Spectra at 25 and 35 °C showed similar chemical shifts, but with a slightly reduced peak dispersion compared with those at 45 °C, indicating that the structure was largely maintained over this temperature range. Therefore, the structure was calculated from spectra at 45 °C because of the narrower line width and slightly improved spectral dispersion. A pH of 5 rather than a higher pH was used to ensure that all exchangeable protons remained visible. At higher pH some peaks showed broadening as a consequence of exchange with the solvent. To confirm that the peptide structures at pH 5 and 7 in micelles were the same, we recorded CD spectra over this pH range; the spectra (not shown) confirmed that the helical content was unchanged over this range.

Distance constraints were obtained from cross-peak volumes in NOESY spectra acquired at 600 MHz. Peak overlap prevented the unambiguous assignment of some cross-peaks, especially for the side chain methyls, where overlap was considerable. The dearth of NOE cross-peaks from the N-terminal region of the peptide (residues 1−3) indicated a larger degree of flexibility in this region relative to the rest of the polypeptide. By contrast, the C-terminus showed strong NOEs through to residue 32. There appears to be considerable mobility in the side chains, with the methyl and aliphatic peaks of many side chains being degenerate. The exceptions were Asp^3 (H^β), Ile^9 (H^γ), Lys^{20} (H^β, H^γ), Glu^{24} (H^β, H^γ), Leu^{26} (H^β), Gly^{27} (H^α), Asn^{28} (H^β), Lys^{30} (H^β), Arg^{31} (H^β), and Lys^{32} (H^β). Generally, there appears to be greater rigidity in the side chains at the C-terminus than the N-terminus, in accord with the stronger NOEs observed for C-terminal residues.

Hydrogen bonds between amide protons and $i - 4$ carbonyl oxygen atoms were included for Ser^{15}, Asp^{17}, Thr^{21}, Val^{22}, Leu^{23}, Ala^{25}, Gly^{27}, Asn^{28}, and Val^{29}. These resonances had amide temperature coefficients ≤4 ppb/°C in magnitude and/or slow amide exchange rates (Table S3 in Supporting Information) (*43*). Hydrogen bond acceptors were defined on the basis of initial structure calculations in X-PLOR. Coupling constants $^3J_{HNH\alpha} < 6$ Hz were observed for Ala^5 and Ala^{12}, giving ϕ angle restraints of $-60 \pm 30°$. A total of 20 ϕ and 3 ψ angle restraints was obtained from analysis of ^1H and ^{13}C chemical shifts using TALOS (Table S3 in Supporting Information).

Solution Structure. Parameters characterizing the final 20 structures and structural statistics of $EqTII_{1-32}$ are summarized in Table 2; this indicates that the structures fit well with experimentally derived distance and angle constraints. The angular order parameters, S, for the backbone ϕ and ψ angles and the side chain χ^1 angles are presented in Figure S7 in Supporting Information. The ϕ and ψ angles are well-ordered ($S_{\phi,\psi} \geq 0.8$) from residues 5−28, indicating that most

Table 2: Structural Statistics for $EqTII_{1-32}$ in DPC-$^2H_{38}$ Micelles at 45 °C

distance restraints	329
intraresidue ($i = j$)	155
sequential ($\|i - j\| = 1$)	93
short ($1 < \|i - j\| < 5$)	81
long	0
dihedral restraints	39
H-bonds	9
energies (kcal mol^{-1})[a]	
E_{NOE}	2.5 ± 1.2
deviations from ideal geometry[b]	
bonds (Å)	0.0040 ± 0.0005
angles (deg)	0.55 ± 0.03
impropers (deg)	0.44 ± 0.05
RMS deviations (Å)[c]	
all heavy atoms	4.96
backbone heavy atoms (N, C$^\alpha$, C′)	4.04
residues 4−13, backbone heavy atoms (N, C$^\alpha$, C′)	1.09
residues 12−28, backbone heavy atoms (N, C$^\alpha$, C′)	1.12
Ramachandran plot[d]	
most favored (%)	89.8
allowed (%)	10.2
additionally allowed (%)	0
disallowed (%)	0

[a] The values for E_{NOE} are calculated from a square well potential with force constants of 50 kcal mol^{-1} Å^2. [b] The values for the bonds, angles, and impropers show the deviations from ideal values based on perfect stereochemistry. [c] RMSD over the backbone heavy atoms (N, C$^\alpha$, C) of all residues. [d] As determined by the program PROCHECK-NMR (*33*) for all residues.

of the peptide structure is well-defined, with only some flexibility at the termini. However, despite the robustness of each individual structure, the pairwise RMSD relative to other structures in the family (4.04 Å over the backbone heavy atoms N, C$^\alpha$, C′) is higher than expected for a relatively well-structured peptide. This may be due to variability in the degree of curvature in the polypeptide chain across the structured regions. If the backbone heavy atom RMSD is calculated for residues within the structured regions, residues 4−13 and 12−28, much smaller values of 1.09 and 1.12 Å, respectively, are obtained.

PROCHECK identified the consensus structure of $EqTII_{1-32}$ as a continuous helix from residues 6−28. However, the NOE data suggest that the helix is a mixture of both α- and 3_{10}-helix. The NOEs of residues 6, 17, 20, 21, and 24 suggest an α-helix, with both $d_{\alpha N}(i, i + 4)$ and $d_{\alpha\beta}(i, i + 3)$ cross-peaks present. By contrast, for residues 7, 10, 12, 15, and 25, $d_{\alpha\beta}(i, i + 3)$, but not $d_{\alpha N}(i, i + 4)$, cross-peaks are present, suggesting a 3_{10}-helix. Medium-range NOEs from other residues are too overlapped to be identified unambiguously. Figure 7 shows a stereoview of the family of 20 structures superimposed over the backbone of residues 10−28, ribbon diagrams of both sides of the closest to mean structure, and a surface diagram of the closest to mean structure with the hydrophobic residues marked in green, hydrophilic residues in red, and charged residues in blue. It can be seen that the central helix is well-defined across the family, but there is slightly more variability in the N-terminal end than the C-terminal. Analysis of ring current shifts in MOLMOL (*34*) using the Haigh−Mallion method indicated that residues 13 and 19 were most affected by upward and downward ring current shifts, respectively, from Phe16.

The amphipathic nature of the helical region (residues 6−28) is illustrated in Figure 7C. One exception is Ser15, a polar residue appearing in the middle of the hydrophobic face, which nevertheless showed $d_{\alpha\beta}(i, i + 3)$ NOE cross-peaks typical of a helical structure. In native EqTII, Ser15 is the first residue of the N-terminal helix and is oriented toward the solvent and away from the β-sheet. Residues $i + 3$ and $i + 4$ are Ile18 and Leu19, and there is no indication of N-capping interactions in the structure.

Micelle Insertion. The orientation of $EqTII_{1-32}$ in DPC-$^2H_{38}$ micelles was investigated using paramagnetic agents. The changes in relative amplitude of the NOE cross-peaks at different concentrations of Mn^{2+} and 5-d-SPPC are shown in Figure S8 in Supporting Information. At high Mn^{2+} ratios, cross-peak intensities of residues 5, 7, 11, 13, and 17 were reduced to zero, indicating high solvent exposure, whereas residues 18, 19, 22, 23, and 26 were less affected, indicating some shielding from the solvent. The effect of 5-d-SPPC is less distinct than Mn^{2+}, with many residues throughout the peptide being affected. Because of spectral overlap the changes in intensity of residues 1, 2, 3, 4, 8, 9, 12, 14, 20, 27, 30, 31, and 32 could not be determined. Figure 7D shows a surface diagram of the closest to average structure with the residues most affected by Mn^{2+} in dark blue, through to the least affected in light blue. Undetermined residues are shown in gray. The combined results from the Mn^{2+} and 5-d-SPPC titrations imply that the peptide lies on the surface of the micelle rather than being buried within it.

DISCUSSION

Pore formation by the actinoporins is a multistage process, with initial membrane binding via the aromatic-rich region, followed by translocation of the N-terminal helical region from the bulk of the protein to the lipid membrane and, finally, insertion into the bilayer to form a functional pore. Cysteine-scanning mutagenesis of the region encompassing residues 10−28 of EqTII showed that this region is α-helical in the membrane, making the helix roughly two turns longer than in the native structure (residues 15−26), and that it lies on the water−lipid interface initially and then inserts into the membrane to line the pore interior, forming an angle of around 20° with the bilayer normal (*13*) (Figure 1B). The functional tetrameric pore is almost certainly a toroidal protein−lipid pore, and importantly, actinoporins with the N-terminus removed do not lyse HRBC (*19*, *23*). In this study we have investigated the structure and lytic activity of peptide fragments from the N-terminus of EqTII with the aim of dissecting the role of the N-terminal region versus the rest of the protein in pore formation.

Light scattering, FTIR, permeabilization, and hemolytic assays of the three N-terminal peptides of EqTII, $EqTII_{11-29}$, $EqTII_{11-32}$, and $EqTII_{1-32}$, have shown that, without the remainder of EqTII to assist in membrane interaction or stabilization, the peptides have a markedly decreased activity, lack of secondary structure in nonlipidic environments, and a higher propensity to aggregate in solution than the full-length protein. This increased likelihood to aggregate suggests that the β-sandwich structure of EqTII plays a role in solubilizing the N-terminal region. In the presence of lipid micelles, however, peptide aggregation was reduced and there was an increase in helical structure, suggesting a preference for a more membrane-like environment.

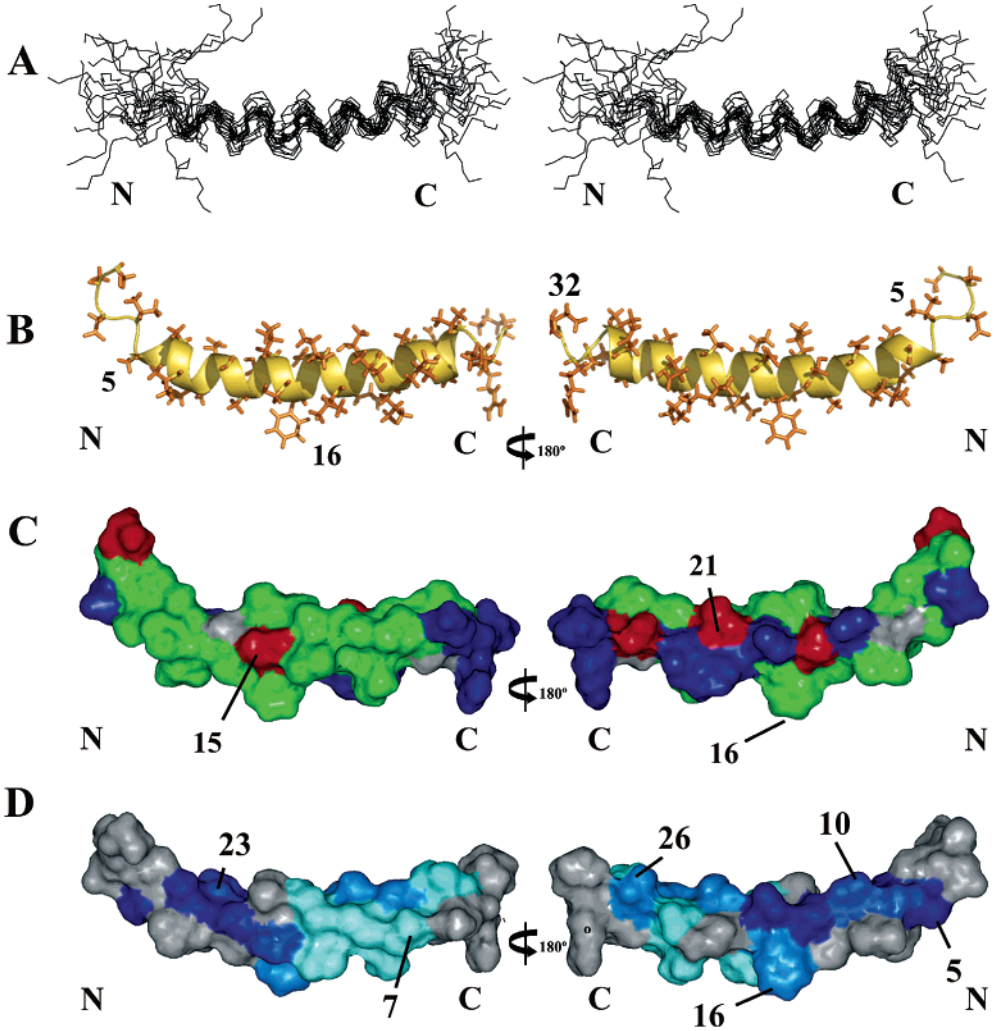

FIGURE 7: Structure of $EqTII_{1-32}$ in DPC-$^2H_{38}$ micelles. (A) Stereoview of the family of 20 final structures, superimposed over backbone heavy atoms from residues 10−28 and the closest to mean structure shown in a (B) ribbon diagram with side chains shown and as a Connolly surface diagram with the (C) residues colored by hydrophobicity: nonpolar residues in green (Ala, Ile, Val, Phe, Leu), polar residues in red (Ser, Thr, Asn), charged residues in blue (Asp, Arg, Glu, Lys), and other residues in gray (Gly), and (D) effect of the solvent- exposed paramagnetic probe, Mn^{2+}, with blue shading indicating the degree of exposure (most exposed residues in dark blue, least affected in light blue). Residues that could not be determined are shown in gray. The letters N and C refer to the amino and carboxyl termini, respectively.

The hemolytic activity of all three peptides was negligible, although some lytic activity against LUVs was detected, with the highest activity occurring at basic pH. The activities of $EqTII_{11-32}$ and $EqTII_{1-32}$ were highest in liposomes containing large fractions of negatively charged lipids, i.e., pure PA and 1:1 PA:PC, respectively. The activity of $EqTII_{11-29}$ against LUVs of either lipid was negligible. Differences in charge between $EqTII_{11-32}$ and $EqTII_{1-32}$ and the absence of the KRK sequence in $EqTII_{11-29}$ affect how the peptides permeabilize HRBC or LUVs, suggesting that the interaction with liposomes containing a net negative charge is due at least partly to electrostatic interactions. The greatly diminished activity of the peptides relative to EqTII may be due to their inability to orient correctly. Although all three peptides are longer than the α-helical region of the N-terminus in native EqTII, the bulk of EqTII may be required to anchor the N-terminal peptide in the correct orientation or to associate the peptides in the membrane prior to oligomerization and pore formation.

As the peptides $EqTII_{11-32}$ and $EqTII_{1-32}$ showed some permeabilizing activity, we investigated their structures by NMR. In aqueous and DMSO solutions, $EqTII_{11-32}$ did not adopt a stable conformation, although its backbone chemical shifts were consistent with slight helical propensity in DMSO. $EqTII_{1-32}$ in aqueous solution also showed a lack of peak dispersion indicative of an absence of secondary structure, but, upon addition of TFE or in DPC-$^2H_{38}$ micelles, the spectra became more dispersed and numerous medium-range cross-peaks were evident in NOESY spectra, indicative of stable helical structure. The peptide structure was more stable in DPC-$^2H_{38}$ micelles than in aqueous TFE, and since micelles are better mimics of biological membranes, we determined the structure of $EqTII_{1-32}$ in this environment.

$EqTII_{1-32}$ in DPC-$^2H_{38}$ micelles is helical from residue 6 to residue 28, making it nearly three turns longer than the corresponding α-helix in the native protein (residues 15−26) (*6*−*8*) at the N-terminus and slightly longer at the C-terminus. In contrast to the helix in full-length EqTII, the N-terminal peptide in DPC-$^2H_{38}$ micelles is not purely α-helical along its entire length, but this may reflect a lack of key NOE restraints caused by peak overlap as much as a genuine departure from α-helical structure. The helix is markedly amphipathic (with the exception of Ser15, which is discussed below) and would be expected to localize at

the interfacial surface region of the micelle rather than the nonpolar core. The effects of paramagnetic agents added to the medium (Mn^{2+}) and the lipid phase (5-d-SPPC) are consistent with a surface location. The peptide structure is better defined at its C-terminus than N-terminus, implying that the C-terminus is more tightly associated with the micelle than the N-terminus.

Ser15 stands out as a polar side chain on the otherwise nonpolar surface of the helix in $EqTII_{1-32}$, lying in close proximity to the side chains of Ile18 and Leu19. In native EqTII, Ser15 is oriented toward the polar solvent and away from the β-sheet; it marks the start of the N-terminal helix, the nearest side chain being that of Ile18. Across the family of actinoporins this sequence position is occupied mainly by Ser or Thr, but in a few cases Gly or Ala is found. Although it is possible that the hydroxy group found in most of the actinoporins confers some benefit in terms of activity, it seems that the principal requirement at position 15 is a small side chain. This may be necessary to accommodate the large structural change associated with transition of the N-terminal region from a hairpin-like structure, in which residues up to residue 10 are largely extended and residues 15−26 are helical, to the membrane-bound form, in which residues 6−28 are entirely helical.

This study has confirmed that the N-terminal region of EqTII is capable of forming a stable helix when separated from the rest of the protein and transferred to a membrane environment. With 23 residues, the helical region of the membrane-associated N-terminus is long enough to span a biological membrane. Given the amphipathic character of this helix, it is likely that its polar face lines the pore and its nonpolar face is oriented toward the acyl region of the membrane as proposed previously (*16*). The majority of the N-terminus (residues 10−28) of EqTII appears to be lining the pore lumen (*13*), as is similarly proposed for the pore formed by another actinoporin, sticholysin II (*44*). As only four EqTII molecules, and thus four N-terminal helices, are required for pore formation, the functional unit is most likely a toroidal protein−lipid pore (*19*, *23*).

Although the N-terminal region of EqTII forms a stable helix long enough to span a lipid bilayer when in a membrane environment, the isolated peptides are only weakly active against LUVs and not hemolytic. This suggests that the rest of the protein plays a key role in pore formation, even though it does not contribute directly to the pore lining. Indeed, full-length EqTII is effective at lower concentrations than smaller antimicrobial peptides that use a single helix for the nonspecific penetration of lipid membranes, e.g., melittin, which shows a transmembrane α-helical structure in lipid bilayers (*45*, *46*), and magainin (*47*). The rest of the protein could be contributing to pore formation by facilitating initial membrane binding via the aromatic cluster (*15*, *17*, *48*) and by stabilizing the tetramer through interactions between neighboring monomers. The requirement for SM for efficient lytic activity could also be mediated by the bulk of the protein. SM is not required for initial membrane binding (*49*, *50*). Our recent ^{19}F NMR studies showed that EqTII binding to PC micelles or bicelles occurred in the absence of SM but that further changes were induced by the addition of SM, which were consistent with a direct effect of SM on EqTII (*48*). Interaction with SM, however, was not sufficient to trigger dissociation of the N-terminal helix from the β-sandwich, at least in micelles and bicelles. It is possible that N-terminal translocation requires a flatter bilayer surface as found in LUVs or cell membranes and/or that it only occurs upon tetramerization.

While this paper was under review, a study by Casallanovo et al. (*52*) was published of peptides derived from the N-terminal sequence of sticholysin II, an actinoporin from *Stichodactyla helianthus*. They also observed a huge reduction of lytic activity on red blood cells and found that these peptides adopted a helical structure in aqueous TFE, although high-resolution structures were not determined.

ACKNOWLEDGMENT

We thank Dr. David Keizer (WEHI) for assistance with structure calculations, Dr. Shenggen Yao (WEHI) for advice on translational diffusion measurements, and Dr. Manuela Coraiola for assistance with FTIR data.

SUPPORTING INFORMATION AVAILABLE

NMR data referred to in the text. This material is available free of charge via the Internet at http://pubs.acs.org.

REFERENCES

1. Anderluh, G., and Maček, P. (2002) Cytolytic peptide and protein toxins from sea anemones (Anthozoa: Actiniaria), *Toxicon 40*, 111−124.
2. Belmonte, G., Pederzolli, C., Maček, P., and Menestrina, G. (1993) Pore formation by the sea anemone cytolysin equinatoxin II in red blood cells and model lipid membranes, *J. Membr. Biol. 131*, 11−22.
3. Michaels, D. W. (1979) Membrane damage by a toxin from the sea anemone *Stoichactis helianthus*. I. Formation of transmembrane channels in lipid bilayers, *Biochim. Biophys. Acta 555*, 67−78.
4. Varanda, W., and Finkelstein, A. (1980) Ion and nonelectrolyte permeability properties of channels formed in planar lipid bilayer membranes by the cytolytic toxin from the sea anemone, *Stoichactis helianthus*, *J. Membr. Biol. 55*, 203−211.
5. Tejuca, M., Dalla Serra, M., Ferreras, M., Lanio, M. E., and Menestrina, G. (1996) Mechanism of membrane permeabilization by sticholysin I, a cytolysin isolated from the venom of the sea anemone *Stichodactyla helianthus*, *Biochemistry 35*, 14947−14957.
6. Zhang, W., Hinds, M. G., Anderluh, G., Hansen, P. E., and Norton, R. S. (2000) Sequence-specific resonance assignments of the potent cytolysin equinatoxin II, *J. Biomol. NMR. 18*, 281−282.
7. Hinds, M. G., Zhang, W., Anderluh, G., Hansen, P. E., and Norton, R. S. (2002) Solution structure of the eukaryotic pore-forming cytolysin equinatoxin II: Implications for pore formation, *J. Mol. Biol. 315*, 1219−1229.
8. Athanasiadis, A., Anderluh, G., Maček, P., and Turk, D. (2001) Crystal structure of the soluble form of equinatoxin II, a pore-forming toxin from the sea anemone *Actinia equina*, *Structure 9*, 341−346.
9. Anderluh, G., Barlič, A., Potrich, C., Maček, P., and Menestrina, G. (2000) Lysine 77 is a key residue in aggregation of equinatoxin II, a pore-forming toxin from sea anemone *Actinia equina*, *J. Membr. Biol. 173*, 47−55.
10. Poklar, N., Fritz, J., Maček, P., Vesnaver, G., and Chalikian, T. V. (1999) Interaction of the pore-forming protein equinatoxin II with model lipid membranes: a calorimetric and spectroscopic study, *Biochemistry 38*, 14999−15008.
11. Menestrina, G., Cabiaux, V., and Tejuca, M. (1999) Secondary structure of sea anemone cytolysins in soluble and membrane bound form by infrared spectroscopy, *Biochem. Biophys. Res. Commun. 254*, 174−180.
12. Anderluh, G., Barlič, A., Podlesek, Z., Maček, P., Pungerčar, J., Gubenšek, F., Zecchini, M. L., Dalla Serra, M., and Menestrina, G. (1999) Cysteine-scanning mutagenesis of an eukaryotic pore-forming toxin from sea anemone: topology in lipid membranes, *Eur. J. Biochem. 263*, 128−136.
13. Malovrh, P., Viero, G., Dalla Serra, M., Podlesek, Z., Lakey, J. H., Maček, P., Menestrina, G., and Anderluh, G. (2003) A novel mechanism of pore formation: membrane penetration by the N-terminal amphipathic region of equinatoxin, *J. Biol. Chem. 278*, 22678−22685.

14. Malovrh, P., Barlič, A., Podlesek, Z., Maček, P., Menestrina, G., and Anderluh, G. (2000) Structure−function studies of tryptophan mutants of equinatoxin II, a sea anemone pore-forming protein, *Biochem. J. 346*, 223−232.
15. Hong, Q., Gutiérrez-Aguirre, I., Barlič, A., Malovrh, P., Kristan, K., Podlesek, Z., Maček, P., Turk, D., González-Mañas, J. M., Lakey, J. H., and Anderluh, G. (2002) Two-step membrane binding by equinatoxin II, a pore-forming toxin from the sea anemone, involves an exposed aromatic cluster and a flexible helix, *J. Biol. Chem. 277*, 41916−41924.
16. Belmonte, G., Menestrina, G., Pederzolli, C., Krizaj, I., Gubenšek, F., Turk, T., and Maček, P. (1994) Primary and secondary structure of a pore-forming toxin from the sea anemone, *Actinia equina* L., and its association with lipid vesicles, *Biochim. Biophys. Acta 1192*, 197−204.
17. Kristan, K., Podlesek, Z., Hojnik, V., Gutiérrez-Aguirre, I., Gunčar, G., Turk, D., González-Mañas, J. M., Lakey, J. H., Maček, P., and Anderluh, G. (2004) Pore formation by equinatoxin, a eukaryotic pore-forming toxin requires a flexible N-terminal region and a stable β-sandwich, *J. Biol. Chem. 279*, 46509−46517.
18. Parker, M. W., and Feil, S. C. (2005) Pore-forming protein toxins: from structure to function, *Prog. Biophys. Mol. Biol. 88*, 91−142.
19. Anderluh, G., Dalla Serra, M., Viero, G., Guella, G., Maček, P., and Menestrina, G. (2003) Pore formation by equinatoxin II, a eukaryotic protein toxin, occurs by induction of nonlamellar lipid structures, *J. Biol. Chem. 278*, 45216−45223.
20. Bonev, B. B., Lam, Y.-H., Anderluh, G., Watts, A., Norton, R. S., and Separovic, F. (2003) Effects of the eukaryotic pore-forming cytolysin equinatoxin II on lipid membranes and the role of sphingomyelin, *Biophys. J. 84*, 2382−2392.
21. Tamm, L. K., and Tatulian, S. A. (1997) Infrared spectroscopy of proteins and peptides in lipid bilayers, *Q. Rev. Biophys. 30*, 365−429.
22. MacDonald, R. C., MacDonals, R. I., Menco, B. P., Takeshita, K., Subbarao, N. K., and Hu, L., R. (1991) Small-volume extrusion apparatus for preparation of large, unilamellar vesicles, *Biochim. Biophys. Acta 1061*, 297−303.
23. Alvarez-Valcarcel, C., Dalla Serra, M., Potrich, C., Bernhart, I., Tejuca, M., Martinez, D., Pazos, F., Lanio, M. E., and Menestrina, G. (2001) Effects of lipid composition on membrane permeabilization by sticholysin I and II, two cytolysins of the sea anemone *Stichodactyla helianthus*, *Biophys. J. 80*, 2761−2774.
24. Dalla Serra, M., Bernhart, I., Nordera, P., Di Giorgio, D., Ballio, A., and Menestrina, G. (1999) Conductive properties and gating of channels formed by syringopeptin 25A, a bioactive lipodepsipeptide from *Pseudomonas syringae* pv. *syringae*, in planar lipid membranes, *Mol. Plant−Microbe Interact. 12*, 401−409.
25. Kay, L. E., Keifer, P., and Sarrinen, T. (1992) Pure absorption gradient enhanced heteronuclear single quantum correlation spectroscopy with improved sensitivity, *J. Am. Chem. Soc. 114*, 10663−10665.
26. Sklenar, V., Piotto, M., Leppick, R., and Saudek, V. (1993) Gradient-tailored water suppression for $^{1}H-^{15}N$ HSQC experiments optimized to retain full sensitivity, *J. Magn. Reson., Ser. A 102*, 241−245.
27. Bartels, C., Xia, T.-H., Billeter, M., Güntert, P., and Wüthrich, K. (1995) The program XEASY for computer-supported NMR spectral analysis of biological macromolecules, *J. Biomol. NMR 6*, 1−10.
28. Ludvigsen, S., and Poulsen, F. M. (1992) Positive ϕ-angles in proteins by nuclear magnetic resonance spectroscopy, *J. Biomol. NMR 2*, 227−233.
29. Cornilescu, G., Delaglio, F., and Bax, A. (1999) Protein backbone angle restraints from searching a database for chemical shift and sequence homology, *J. Biomol. NMR 13*, 289−302.
30. Herrmann, T., Güntert, P., and Wüthrich, K. (2002) Protein NMR structure determination with automated NOE assignment using the new software CANDID and the torsion angle dynamics algorithm DYANA, *J. Mol. Biol. 319*, 209−227.
31. Güntert, P., Braun, W., and Wüthrich, K. (1991) Efficient computation of three-dimensional protein structures in solution from nuclear magnetic resonance data using the program DIANA and the supporting programs CALIBA, HABAS and GLOMSA, *J. Mol. Biol. 217*, 517−530.
32. Schwieters, C. D., Kuszewski, J. J., Tjandra, N., and Clore, G. M. (2003) The Xplor-NIH NMR molecular structure determination package, *J. Magn. Reson. 160*, 65−73.
33. Laskowski, R. A., Rullmannn, J. A., MacArthur, M. W., Kaptein, R., and Thornton, J. M. (1996) AQUA and PROCHECK-NMR: programs for checking the quality of protein structures solved by NMR, *J. Biomol. NMR 8*, 477−486.
34. Koradi, R., Billeter, M., and Wüthrich, K. (1996) MOLMOL: a program for display and analysis of macromolecular structures, *J. Mol. Graphics 14*, 51−55.
35. Dingley, A. J., Mackay, J. P., Chapman, B. E., Morris, M. B., Kuchel, P. W., Hambly, B. D., and King, G. F. (1995) Measuring protein self-association using pulsed-field-gradient NMR spectroscopy: application to myosin light chain 2, *J. Biomol. NMR 6*, 321−328.
36. Yao, S., Howlett, G. J., and Norton, R. S. (2000) Peptide self-association in aqueous trifluoroethanol monitored by pulsed field gradient NMR diffusion measurements, *J. Biomol. NMR 16*, 109−119.
37. MacRaild, C. A., Howlett, G. J., and Gooley, P. R. (2004) The structure and interactions of human apolipoprotein C−II in dodecyl phosphocholine, *Biochemistry 43*, 8084−8093.
38. Lindberg, M., Jarvet, J., Langel, U., and Graeslund, A. (2001) Secondary structure and position of the cell-penetrating peptide transportan in SDS micelles as determined by NMR, *Biochemistry 40*, 3141−3149.
39. Pederzolli, C., Belmonte, G., Dalla Serra, M., Maček, P., and Menestrina, G. (1995) Biochemical and cytotoxic properties of conjugates of transferrin with equinatoxin II, a cytolysin from a sea anemone, *Bioconjugate Chem. 6*, 166−173.
40. le Maire, M., Champeil, P., and Møller, J. V. (2000) Interaction of membrane proteins and lipids with solubilizing detergents, *Biochim. Biophys. Acta 1508*, 86−111.
41. Lapham, J., Rife, J. P., Moore, P. B., and Crothers, D. M. (1997) Measurement of diffusion constants for nucleic acids by NMR, *J. Biomol. NMR 10*, 255−262.
42. Seavey, B. R., Farr, E. A., Westler, W. M., and Markley, J. L. (1991) A relational database for sequence-specific protein NMR data, *J. Biomol. NMR 1*, 217−236.
43. Baxter, N. J., and Williamson, M. P. (1997) Temperature dependence of ^{1}H chemical shifts in proteins, *J. Biomol. NMR 9*, 359−369.
44. Mancheño, J. M., Martin-Benito, J., Martinez-Ripoll, M., Gavilanes, J. G., and Hermoso, J. A. (2003) Crystal and electron microscopy structures of sticholysin II actinoporin reveal insights into the mechanism of membrane pore formation, *Structure 11*, 1319−1328.
45. Dempsey, C. E. (1990) The actions of melittin on membranes, *Biochim. Biophys. Acta 1031*, 143−161.
46. Smith, R., Separovic, F., Milne, T. J., Whittaker, A., Bennett, F. M., Cornell, B. A., and Makriyannis, A. (1994) Structure and orientation of the pore-forming peptide, melittin, in lipid bilayers, *J. Mol. Biol. 241*, 456−466.
47. Bechinger, B. (1997) Structure and functions of channel-forming polypeptides: magainins, cecropins, melittin and alamethicin, topical review, *J. Membr. Biol. 156*, 197−211.
48. Anderluh, G., Razpotnik, A., Podlesek, Z., Maček, P., Separovic, F., and Norton, R. S. (2005) Interaction of the eukaryotic pore-forming cytolysin equinatoxinII with model membranes: ^{19}F NMR studies, *J. Mol. Biol. 347*, 27−39.
49. Caaveiro, J. M. M., Echabe, I., Gutiérrez-Aguirre, I., Nieva, J. L., Arrondo, J. L. R., and González-Mañas, J. M. (2001) Differential interaction of equinatoxin II with model membranes in response to lipid composition, *Biophys. J. 80*, 1343−1353.
50. Maček, P., Zecchini, M., Pederzolli, C., Dalla Serra, M., and Menestrina, G. (1995) Intrinsic tryptophan fluorescence of equinatoxin II, a pore-forming polypeptide from the sea anemone *Actinia equina*, monitors its interaction with lipid membranes, *Eur. J. Biochem. 234*, 329−335.
51. Wishart, D. S., Sykes, B. D., and Richards, F. M. (1992) The chemical shift index: a fast and simple method for the assignment of protein secondary structure through NMR spectroscopy, *Biochemistry 31*, 1647−1651.
52. Casallanovo, F., de Oliveira, F. J., de Souza, F. C., Ros, U., Martinez, Y., Penton, D., Tejuca, M., Martinez, D., Pazos, F., Pertinhez, T. A., Spisni, A., Cilli, E. M., Lanio, M. E., Alvarez, C., Schreier, S. (2005) Model peptides mimic the structure and function of the N-terminus of the pore-forming toxin sticholysin II, *Biopolymers* (in press).

BI052166O